

FAR-INFRARED AND SUBMILLIMETER POLARIZATION OF OMC-1: EVIDENCE FOR MAGNETICALLY REGULATED STAR FORMATION¹

D. A. SCHLEUNING

Department of Astronomy and Astrophysics, University of Chicago, Chicago, IL 60637; david@oddjob.uchicago.edu

Received 1997 March 27; accepted 1997 September 8

ABSTRACT

This paper presents large-scale polarization maps ($8' \times 8'$) of the Orion molecular cloud (OMC-1) at far-infrared ($100\ \mu\text{m}$; $35''$ resolution) and submillimeter ($350\ \mu\text{m}$; $18''$ resolution) wavelengths. The magnetic field shows a pinch at scales less than $0.5\ \text{pc}$ with a centroid that is on the OMC-1 ridge, a site of high-mass star formation. We infer that gravitational collapse pulled the magnetic field into an hourglass shape. We estimate that the magnetic, kinetic, and gravitational energies are in equipartition on the ridge and that the magnetic energy dominates in the surrounding ambient envelope. We consider a model in which the ridge and thus high-mass stars gravitationally collapsed out of a cloud that was initially supported by the magnetic field. At flux peaks, there is a reduction in the percent polarization. This effect is discussed in relation to temperature, optical depth, and wavelength.

Subject headings: H II regions — infrared: ISM: continuum — ISM: individual (Orion Nebula) — ISM: magnetic fields — polarization — stars: formation

1. INTRODUCTION

The Orion Molecular Cloud (OMC-1) is the closest site of OB star formation. Various theories of star formation have in common a picture of gravitational collapse that is influenced by the magnetic field (Mouschovias 1995; Heiles et al. 1993; McKee et al. 1993; Shu, Adams, & Lizano 1987). Shu et al. (1987) have developed a bimodal model of star formation: high-mass stars form in supercritical (gravitationally dominated) clouds, and low-mass stars form in subcritical (magnetically dominated) clouds. Direct observations of the magnetic field structure following gravitational collapse have been limited to comparisons of the field strength in the envelopes (Zeeman splitting of H I absorption lines) and cores (OH and H₂O masers) of clouds (e.g., the Barnard I cloud; Crutcher et al. 1994). The data presented here attempt to trace the shape of the magnetic field from the star-forming cores into the surrounding envelope.

Early attempts to measure the far-infrared polarization of OMC-1 gave upper limits for the polarization of $2\% \pm 2\%$ from the Kuiper Airborne Observatory (KAO) (Gull et al. 1978) and, later, a detection of $2.2\% \pm 0.4\%$ from a balloon-borne experiment (Cudlip et al. 1982). Instruments developed at the University of Chicago have led to successive improvements in the number and accuracy of the measurements of far-infrared to submillimeter polarization (Hildebrand, Dragovan, & Novak 1984; Dragovan 1986; Gonatas et al. 1990; Hildebrand et al. 1995; Schleuning, Dowell, & Platt 1996). Novak et al. (1989) have discussed the polarization mechanism in OMC-1. They conclude that the far-infrared polarization is due to emission from elongated dust grains that have been aligned by the local magnetic field. Therefore, the magnetic field in the plane of the sky is perpendicular to the polarization sampled by our far-infrared and submillimeter measurements.

Largely because of its proximity ($450\ \text{pc}$), OMC-1 has been studied over a broad range of continuum frequencies

and with numerous molecular lines (see review by Genzel & Stutzki 1989). Figure 1 shows the large-scale features in OMC-1, and Figure 2 presents our schematic picture of the cloud along the line of sight. Our maps of far-infrared and submillimeter continuum sample warm and cool dust throughout the cloud, which for the most part is optically thin. The star, $\Theta^1\ \text{Ori C}$, within the Trapezium powers the bright H II region, M42, which is prominent in optical and radio free-free emission (e.g., $6\ \text{cm}$ continuum emission; Johnston et al. 1983). Because the optical nebula is visible, high column density dust, traced by $350\ \mu\text{m}$ emission (D. C. Lis, T. R. Hunter, E. Serabyn, N. Wang, D. J. Benford, & T. G. Phillips 1997, private communication), must lie behind the H II region. In the background molecular cloud, the KL Nebula (hereafter KL) is the flux peak from far-infrared to millimeter wavelengths on the OMC-1 “ridge.” The ridge has linear structure oriented north-south and is offset from the M42 H II region. A submillimeter peak, “KHW,” with equal mass but lower dust temperature, is found $90''$ south of KL along the ridge (Keene, Hildebrand, & Whitcomb 1982). The “dark bay” is in the foreground of the H II region, and the “bar” is seen edge-on on the southern edge of the nebula.

Section 2 presents the observations and discusses systematic effects. Section 3 presents the polarization results with respect to features in the OMC-1 cloud and empirical relationships of the polarization with respect to optical depth, temperature, and wavelength. Section 4 offers a model of the magnetic field geometry. Using energy and length scale arguments, we suggest a model of magnetically regulated star formation in OMC-1.

2. OBSERVATIONS

The observations were made on the KAO with the far-infrared polarimeter, Stokes (Platt et al. 1991) and at the Caltech Submillimeter Observatory (CSO) with the submillimeter polarimeter, Hertz (Schleuning et al. 1997). In both cases, the observations were made using standard infrared techniques of spatially chopping the secondary mirror ($3\text{--}20\ \text{Hz}$) to remove the large atmospheric background and position switching the telescope ($0.1\ \text{Hz}$) to

¹ Presented as a dissertation to the Department of Astronomy and Astrophysics, University of Chicago, in partial fulfillment of the requirements for the Ph.D. degree.

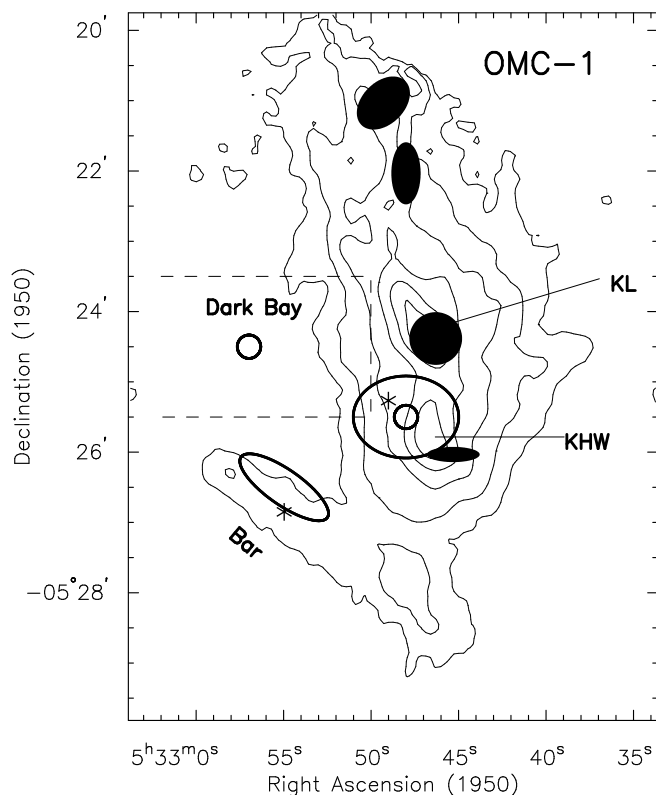


FIG. 1.—A large-scale map of the gas and dust in OMC-1. Thin contours show $350\ \mu\text{m}$ emission measured with $15''$ resolution (D. C. Lis, T. R. Hunter, E. Serabyn, N. Wang, D. J. Benford, & T. G. Phillips 1997, private communication). Dark patches represent deconvolved NH_3 sources (Batra et al. 1983), which bead the $350\ \mu\text{m}$ emission in a north-south orientation (§ 3.2.1). Dark contours give the prominent clumps of the $158\ \mu\text{m}$ $[\text{C II}]$ emission with $60''$ resolution (Stacey et al. 1993). The $[\text{C II}]$ emission is offset from the bar (§ 3.2.3) and KHW (§ 3.2.2) toward the Trapezium. Dashed lines designate the approximate position of the dark bay (§ 3.2.4). The asterisks give the locations of the stars, Θ^1 Ori C (northwestern star) and Θ^2 Ori A (coincident with the bar).

remove offsets. A free-standing wire grid splits the beam into orthogonal components of polarization. The two components are detected by two arrays of ^3He -cooled bolometers, which provide 32 pixels on the sky. The photometric signal is the sum of the signals from detectors in each of the arrays. The polarization signal is the difference over the sum of the signals. A half-wave plate, stepped in six positions separated by 30° , is used to analyze the polarization. Correlated noise due to fluctuations of the atmospheric attenuation is effectively eliminated from the polarization signal.

2.1. KAO Observations

The far-infrared ($100\ \mu\text{m}$) observations were made on three KAO flights in 1993 December. The measurements have $35''$ resolution (FWHM) with a beam spacing of $37''.3$. The bandpass was determined by interference filters made of low-pass capacitive mesh ($80\ \mu\text{m}$) and high-pass inductive mesh ($125\ \mu\text{m}$) filters. The spatial chopping had a throw of $9'$ at an angle that rotated on the sky from 36° to 65° (measured counterclockwise from north). Following Platt et al. (1991), a multiple linear regression was used on data from W3, NGC 2024, and OMC-1 to determine a uniform telescope polarization ($0.91\% \pm 0.02\%$) and instrument polarizations for each pixel (median value of 0.3% with a standard deviation of 0.1%).

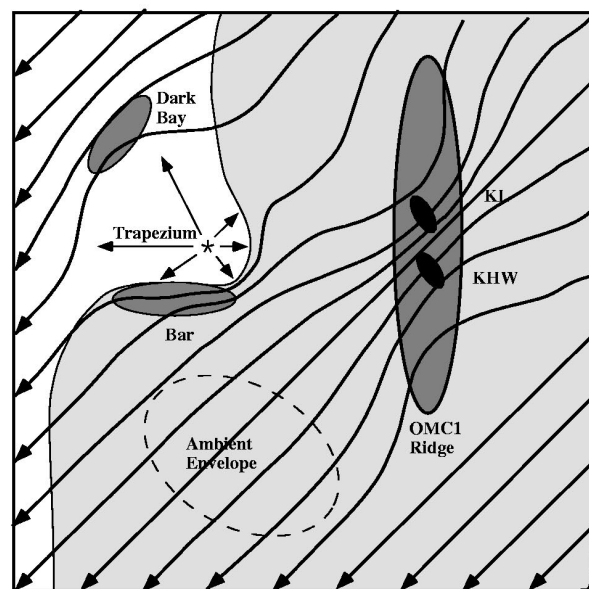


FIG. 2.—A schematic representation of OMC-1 along the line of sight. (The observer is to the left.) The Trapezium excites the M42 H II region (thin arrows), which has blistered in front of the OMC-1 cloud. The bar (§ 3.2.3) is a limb-brightened clump below the H II region, and the dark bay (§ 3.2.4) is in the foreground of the nebula. KL and KHW are clumps within the OMC-1 ridge in the background molecular cloud. Thin lines represent our model of the magnetic field. In the ambient envelope (dashed ellipse), the magnetic field lines are straight (§ 3.3.1) with a field strength similar to the field measured in the dark bay (§ 4.1). The field has bulged around the M42 H II region and is gravitationally pulled into an hourglass shape in the background molecular cloud (§ 4.2).

The telescope polarization, caused by the dichroic tertiary mirror, was confirmed by measurements on the ground with a blackbody source at the position of the secondary mirror. The polarization modulation efficiency was measured to be 89% using a highly polarized source at the position of the secondary, and it has been applied to all of the results.

Systematic errors can result from spatially chopping into flux in the reference beams (Novak et al. 1997; Schleuning et al. 1997). Using their nomenclature, we define the “source” and “reference” positions to have intrinsic fluxes, F_s and F_r , polarizations, P_s and P_r , and position angles, Φ_s and Φ_r . The spatially differencing polarimeter measures an “apparent” flux, F_a , polarization, P_a , and position angle, Φ_a . To determine systematic errors in polarization (ΔP_- , ΔP_+ , and $\Delta\Phi$) (as defined by Schleuning et al. 1997), we assume a reference polarization and estimate the ratio of source to reference-beam flux. By further assuming a reference position angle, the “derived source” polarization (P_{ds} and Φ_{ds}) can be calculated and can be used to further constrain the systematic effect.

Figure 3 shows a subset of data previously presented (Hildebrand et al. 1995; Platt et al. 1995) that satisfy $P_a - \Delta P_- - 2\sigma_p > 0$ (dark vectors), where σ_p is the statistical error. To calculate the reference-beam error, we have estimated the ratio of source to reference flux from a $91\ \mu\text{m}$ map (2.2 resolution) of OMC-1 (Harper 1974), which had larger spatial coverage than our map. The flux distribution is broader to the northeast, causing contamination to our polarization measurements in the southwest corner of Figure 3. The systematic errors were calculated by assuming a reference polarization (P_r) of 6% , which is the most likely

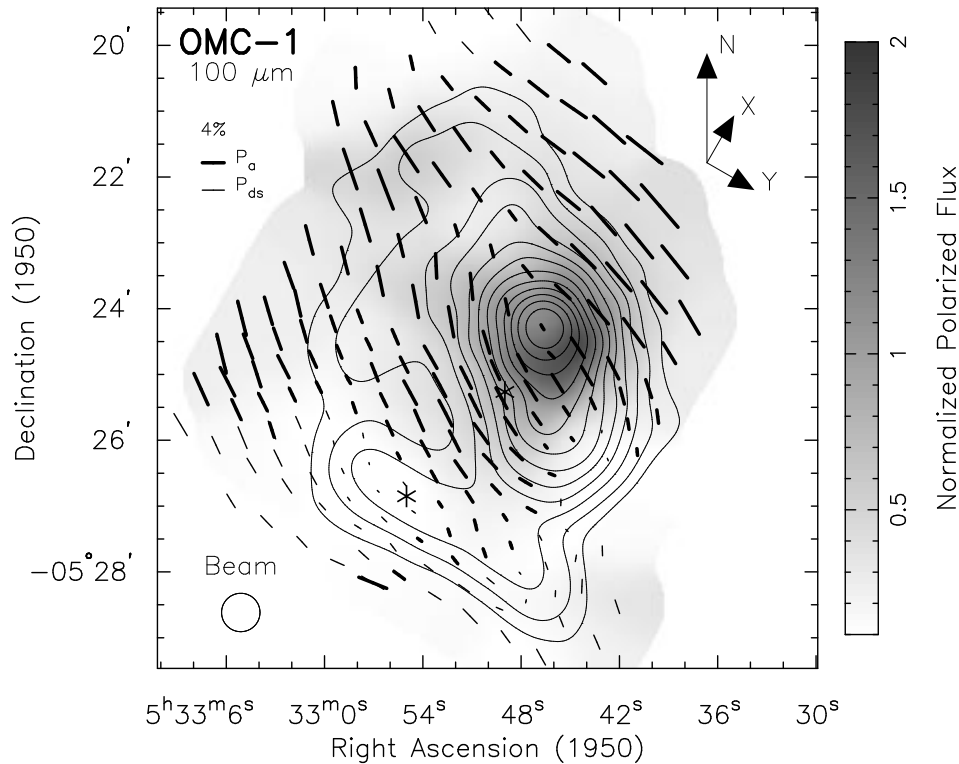


FIG. 3.—The 100 μm apparent and derived source polarization vectors (defined in § 2.1). Dark vectors represent apparent polarization measurements (P_a) that satisfy the criterion ($P_a - \Delta P_- - 2\sigma_p > 0$). Thin vectors represent the derived source polarization (P_{ds}). Contours give the 100 μm photometric flux normalized to unity at KL with levels at 0.06, 0.08, 0.10, 0.13, 0.16, 0.20, 0.25, 0.32, 0.40, 0.50, 0.63, and 0.79. The gray scale represents the polarized flux (polarization multiplied times the normalized flux). Array coordinates (x- and y-axes) are shown relative to north (upper right-hand corner). The asterisks give the locations of the stars, Θ^1 Ori C (northwestern star) and Θ^2 Ori A (coincident with the bar). The 35'' beam size is shown in the lower left-hand corner, and 4% vectors are shown in the upper left-hand corner.

value on the eastern edge of the map. An analysis with a reference polarization of 9% gives similar results. By further assuming a reference position angle (Φ_r) of 30° , the derived source polarization is calculated and shown in Figure 3 (thin vectors). In the southwest corner of the map, few of the apparent polarization measurements satisfy the above criterion, and the derived source polarization has a 90° change in position angle from the apparent polarization. At many positions (e.g., the bar), where the apparent polarization is low, the apparent polarized flux (polarization multiplied times photometric flux) is less than the estimated reference-beam polarized flux ($P_a \times F_a < P_r \times F_r$). This discrepancy leads to a systematic error of $\pm 90^\circ$ in the position angle. Although the uncertainties preclude any interpretation of position angles along the bar, it is clear that the percent polarization is low in this region.

For most of the analyses in this work, we consider a subset of the data that satisfies the following requirements: (1) $P_a - \Delta P_- - 2\sigma_p > 0$, (2) $P_a > 3\sigma_p$, (3) $\phi_a - \phi_{ds} < 10^\circ$, and (4) $\delta > -5^\circ 26' 30''$, where δ is the declination of the measurement. The final requirement removes a few scattered points in the bar. Figure 4 shows the apparent polarization vectors that satisfy the above requirements, rotated by 90° to show the implied magnetic field. All of the data have been tabulated in a separate paper (Dotson et al. 1998), which archives all of the KAO polarization data.

2.2. CSO Observations

Figure 5 shows the submillimeter (350 μm) polarization vectors, flux contours, and polarized flux (gray scale). The

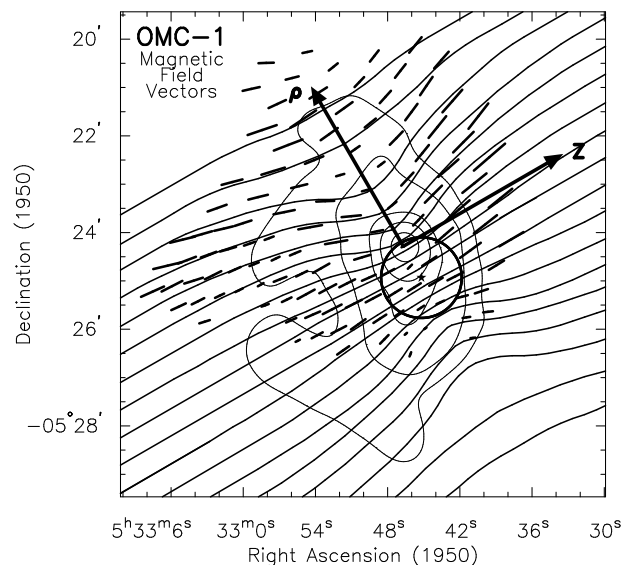


FIG. 4.—The 100 μm magnetic field vectors. The polarization data set has been reduced using the criteria discussed in § 2.1 to remove measurements with large systematic and statistical errors. The vectors have been rotated 90° to represent the inferred magnetic field direction. The z- and ρ -axes represent our symmetry coordinate system and are drawn with a length of 0.5 pc (240''). The sketched magnetic field lines (solid lines; discussed in § 3.3.2) show a symmetrical distortion at scales less than $R_{\text{pinch}} = 0.5$ pc and are centered about a point (star) that is 0.1 pc (45'') southwest of KL. The vectors are uniform across the ridge at scales less than $R_{\text{ridge}} = 0.1$ pc (45''); small circle) and show no local pinching around KL or KHW.

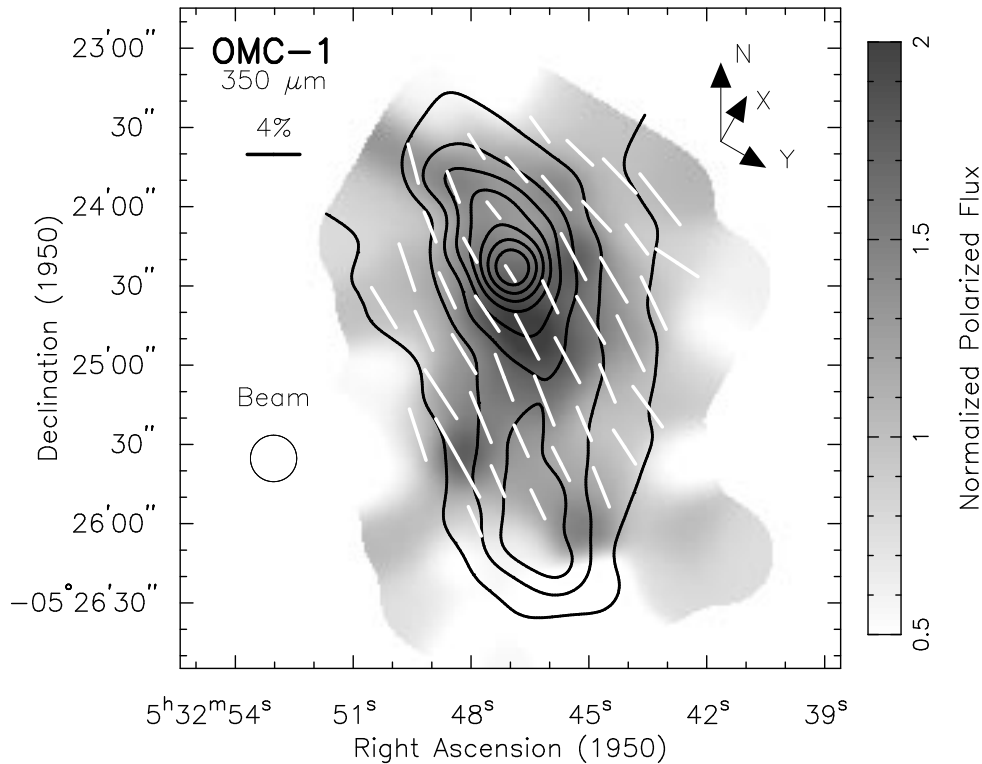


FIG. 5.—The 350 μm polarization (E -vectors). Vectors show the 350 μm polarization. Contours give the normalized 350 μm flux with levels at 0.2, 0.3, 0.4, 0.5, 0.6, 0.7, 0.8, and 0.9. The gray scale gives the 350 μm polarized flux (§ 2.2). The 18'' beam size is shown in the lower left-hand corner, and a 4% vector is shown in the upper left-hand corner.

350 μm data were taken 1995 October 30–1995 November 1. The spatial chopping was in azimuth with a throw of 6'. On the sky, the direction of the chop was roughly east-west. The data have been tabulated and systematic errors have been discussed in a separate paper (Schleuning et al. 1997).

3. RESULTS

The 100 μm data set contains 210 sky positions, 74 of which are at oversampled positions. After removing data of low statistical significance or with large systematic errors due to flux in the reference beam (see § 2.1), we consider the remaining 92 independent measurements and 32 additional measurements in oversampled sky positions. The 100 μm polarization has a median value of 4.2%. The single measurement with a polarization greater than 8% has an apparent polarization of $10.25\% \pm 0.43\% \pm_{4.3}^{1.1}\%$ (statistical and systematic errors, respectively), which is consistent with 8%. Thus, we determine that the 100 μm polarization in OMC-1 ranges from 0% to 8%. The 350 μm data set contains 46 independent measurements with no cut necessary for systematic errors. The 350 μm polarization has a median value of 3.2% and a highest value of 5.8%. The difference of the median and largest polarization between the two data sets is due, in part, to the larger spatial coverage of the 100 μm data (see § 3.1.3).

3.1. The Radial Dependence of Polarization

The polarization in OMC-1 has been observed to decrease radially toward KL at 100 μm (Gonatas et al. 1990), 450 μm (Schleuning et al. 1996), 800 μm (Aitken et al. 1997), and 1.3 mm (Leach et al. 1991). This decrease has been termed a “polarization hole.” Figure 6 shows the polarization, flux, and polarized flux in terms of cuts along

axes defined by the array footprint centered at KL. These cuts avoid some of the flux features in the map, such as KHW and the northeastern extension to KL associated with CS-1 (§ 3.2.1); however, other features, such as the bar and the dark bay, are prominent in the cuts. The distribution of flux shows a smooth decrease away from KL with a FWHM of 45'' at 350 μm . The 350 and 100 μm polarized flux has a considerably broader distribution but has a large-scale trend of increasing values into the OMC-1 ridge. This implies that grains in the ridge of denser material are polarized, and thus our measurements do map the magnetic field in this environment.

The highest polarization (8%) is found well away from KL to the northwest, in a region away from the H II nebula and not associated with any flux features. Bright flux peaks with higher column densities and temperatures have lower polarization, and thus it appears that structures in the polarization map are correlated with structures in the photometric map (see § 3.2). The 100 μm cuts of polarized flux show a local minimum at KL and a peak that is offset 15''–30'' to the south of KL (+ y and $-x$) along the ridge of molecular emission (see gray scale in Figs. 3 and 5). This indicates that KL has an anomalously low polarization compared to the large-scale trend in the OMC-1 cloud. The minimum of polarized flux at KL is more pronounced at 100 μm than at 350 μm .

3.1.1. The Temperature Dependence

Figure 7 shows the polarization as a function of dust temperature (60'' resolution; Werner 1982) and excitation temperature (^{12}CO with 45'' resolution; Bergin et al. 1994). We have considered measurements that are spatially coincident; however, one must recall biases in the temperature

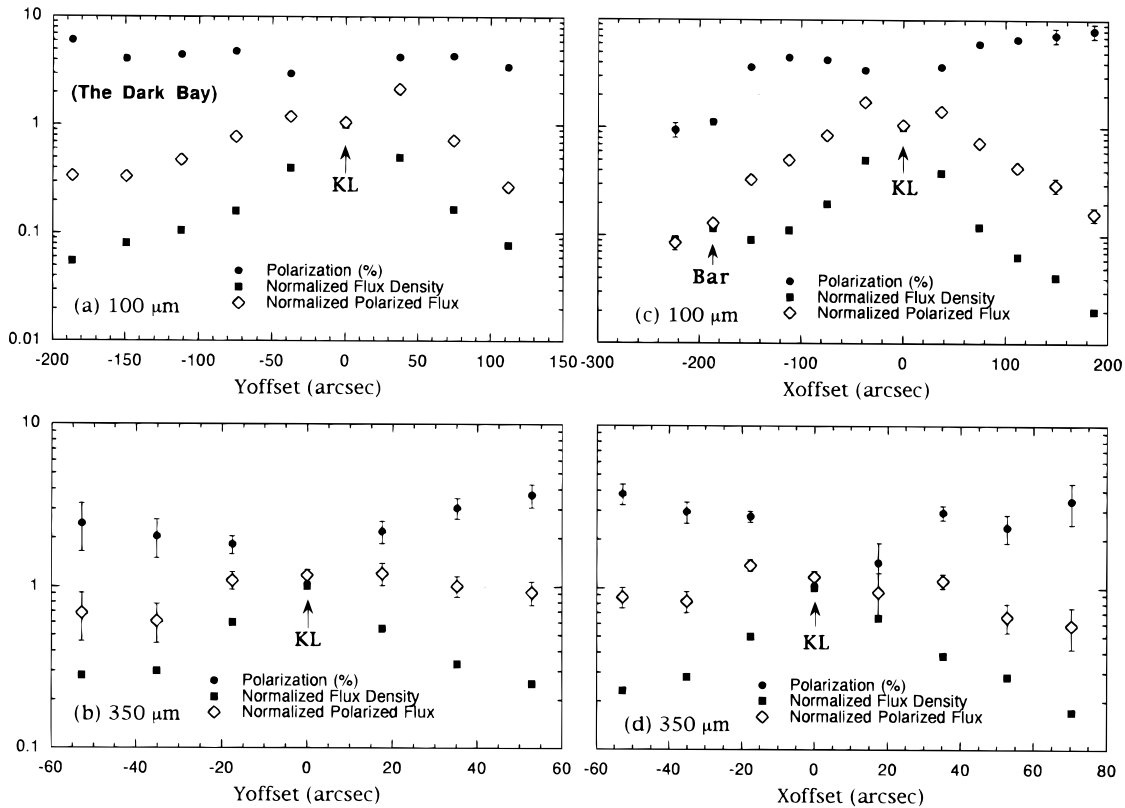


FIG. 6.—Cuts of polarization, flux density, and polarized flux across KL. In the array coordinate system, x is defined as 30° west of north and y is defined as 30° south of west (see Figs. 3 and 5). The polarization (circles) is $1.05\% \pm 0.03\%$ ($100\ \mu\text{m}$) and $1.4\% \pm 0.1\%$ ($350\ \mu\text{m}$) at the KL peak ($x = 0$; $y = 0$). The flux density (squares) at 100 and $350\ \mu\text{m}$ has been normalized to unity at the KL peak. The polarized flux (diamonds) is the polarization multiplied times the normalized flux density. The statistical errors are typically less than the symbol size; (a) $100\ \mu\text{m}$ y -cut, (b) $350\ \mu\text{m}$ y -cut, (c) $100\ \mu\text{m}$ x -cut (across the bar; § 3.2.3), and (d) $350\ \mu\text{m}$ x -cut.

estimates due to gradients along the line of sight, optical depth effects, and molecular line transition biases. An analysis with T_{rot} ($\text{CH}_3\text{C}_2\text{H}$; Bergin et al. 1994) gives results similar to the comparison with excitation temperature.

The maximum polarization for a given temperature appears to decrease with increasing dust or excitation temperature; however, this weak correlation may be caused by other effects that are also radially dependent (e.g., optical depth; § 3.1.2). The dependence of polarization on the ratio $T_{\text{ex}}/T_{\text{d}}$ also shows a decreasing trend (Fig. 7c), which is opposite to what one would expect for paramagnetic relaxation for thermally rotating grains (Davis & Greenstein 1951). For all cases in which we measure polarization, the ratio $T_{\text{ex}}/T_{\text{d}}$ is less than 2. This result gives stronger evidence against Davis-Greenstein alignment (Roberge 1996); however, if the grains are spinning at suprathermal rotational velocities, they can be still be aligned by paramagnetic relaxation (Purcell 1979). Although there is no clear trend in the polarization as a function of temperature, we conclude that grains are efficient polarizers in environments where the gas and dust have roughly the same temperature.

3.1.2. The Optical Depth Dependence

Figure 8 shows the polarization as a function of $100\ \mu\text{m}$ optical depth ($60''$ resolution; Werner 1982) and normalized $350\ \mu\text{m}$ flux density (this work), which both peak at KL. The $100\ \mu\text{m}$ optical depth is directly proportional to the column density of warm dust, and the $350\ \mu\text{m}$ flux on the Rayleigh-Jeans tail of emission traces the column density of

cool dust. The maximum polarization at each optical depth decreases with increasing optical depth.

Gull et al. (1978) first proposed that the low polarization at KL could be due to high opacity. Even for perfect alignment of elongated grains, an opaque region will have equal flux in orthogonal directions on the sky and thus be unpolarized. For a cloud with uniform temperature, density, and grain alignment, the polarization is given by

$$P = \frac{\sinh(\eta\tau)e^{-\tau}}{1 - \cosh(\eta\tau)e^{-\tau}}, \quad (1)$$

where $\tau = \frac{1}{2}(\tau_x + \tau_y)$, x and y are orthogonal directions on the sky, and η is the polarization efficiency [defined by $\Delta\tau_x = (1 + \eta)\Delta\tau$; $\Delta\tau_y = (1 - \eta)\Delta\tau$]. In the limit of low optical depth, equation (1) reduces to $P \sim \eta(1 - \tau)$. The parameter η includes all the information about properties and alignment efficiencies of the grains and thus defines the intrinsic polarization in a uniform cloud. For the $100\ \mu\text{m}$ results shown in Figure 8, the extrapolation to low optical depth gives a maximum polarization of $\sim 8\%$. Using $\eta = 8\%$, we plot equation (1) in Figure 8 and find that the data lie well below this opacity limit. However, the optical depth measurements have a resolution of $60''$ that could smooth over optically thick clumps. At KL, such clumps have been observed (§ 3.2.1). Since the optical depth is wavelength dependent, we can constrain clump models by considering the dependence of the polarization with wavelength (§ 3.1.3).

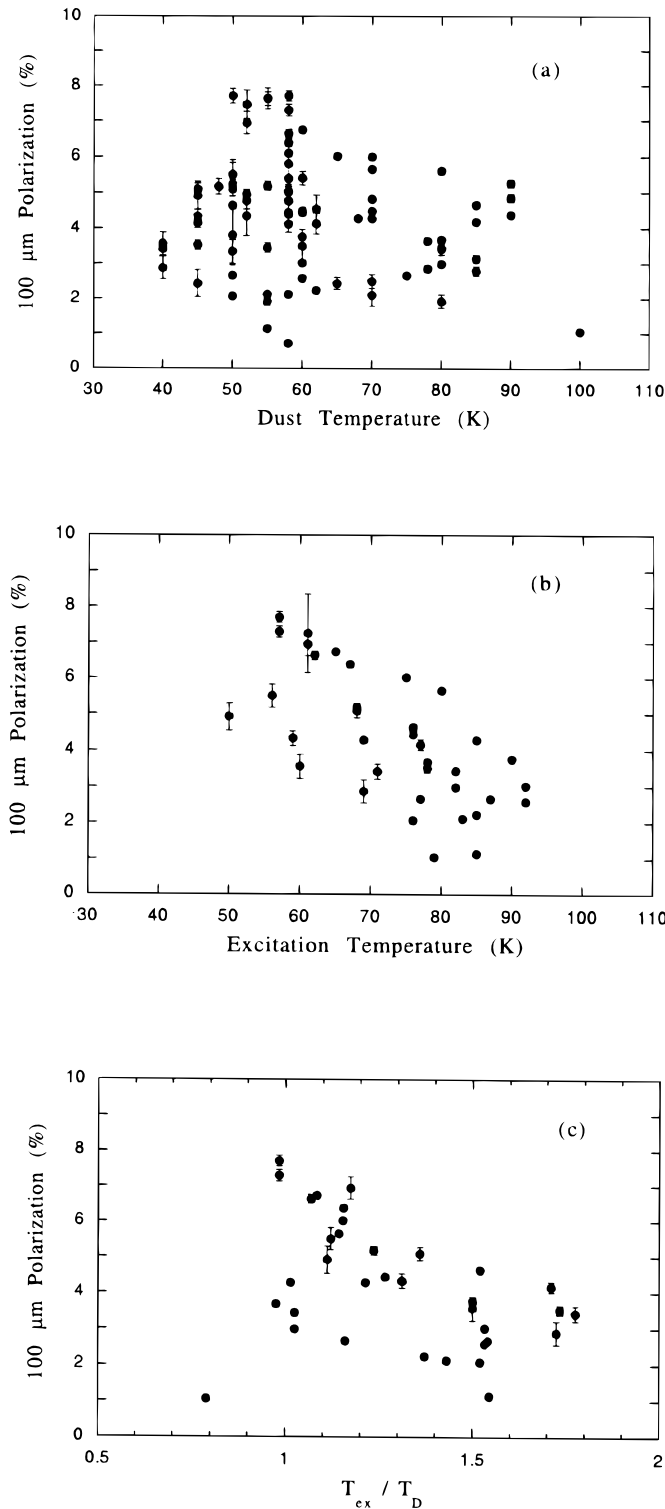


FIG. 7.—Polarization vs. temperature. Independent 100 μm polarization measurements are plotted as a function of (a) dust temperature (T_D) from 50 and 100 μm maps (60" resolution; Werner 1982), (b) excitation temperature (T_{ex}) from the $J = 1 \rightarrow 0$ transition of ^{12}CO (45" resolution; Bergin et al. 1994), and (c) the ratio of T_{ex}/T_D .

3.1.3. The Wavelength Dependence of Polarization

Figure 9 shows the inferred magnetic field direction (polarization vectors rotated by 90°) for the 100 and 350 μm measurements along the OMC-1 ridge. Except where noted below, we find that spatially coincident points have, within the uncertainties, the same position angle and percent

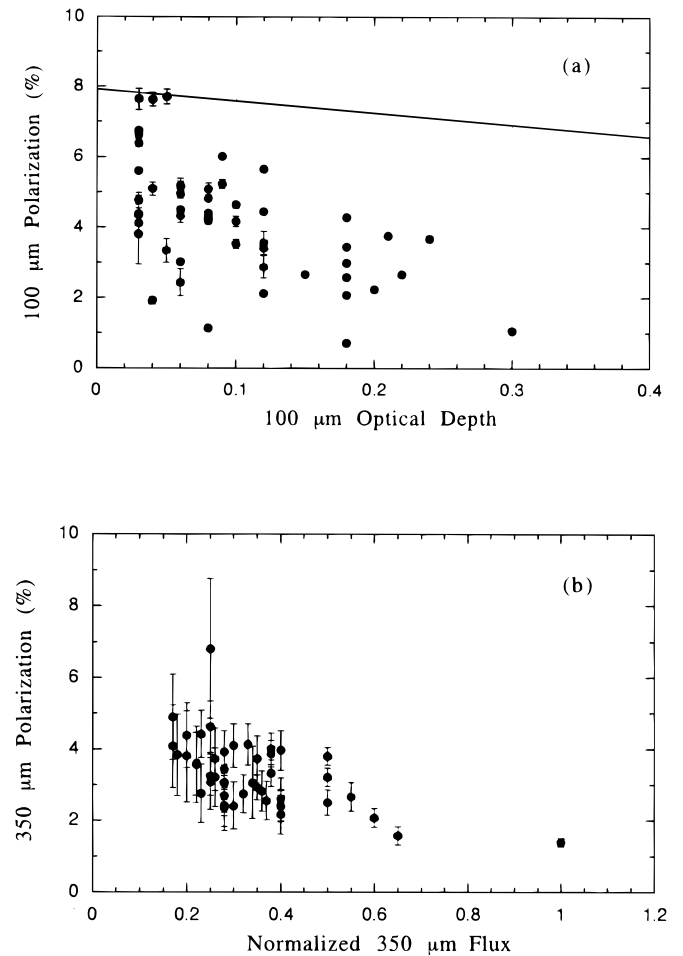


FIG. 8.—Polarization vs. optical depth. (a) Independent 100 μm polarization measurements are plotted as a function 100 μm optical depth (60" resolution; Werner 1982). The line represents eq. (1), using $\eta = 8\%$. (b) The 350 μm polarization is plotted against the normalized 350 μm flux, which traces the column density of cold dust. Error bars give the statistical errors.

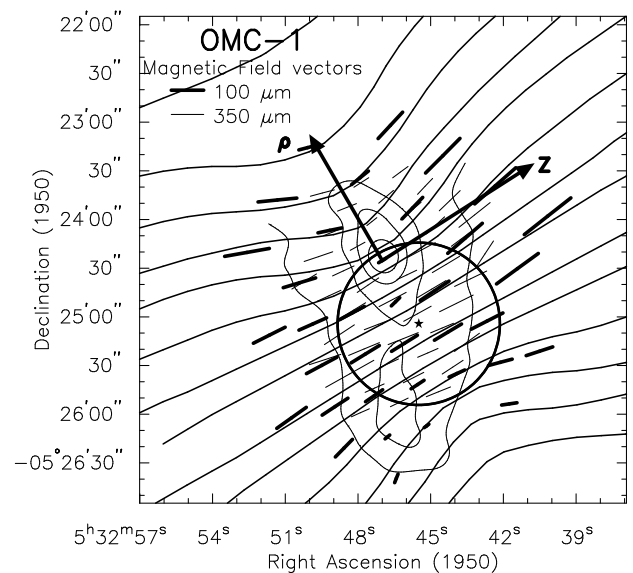


FIG. 9.—Magnetic field vectors along the OMC-1 ridge. Thick vectors represent a subset of the 100 μm polarization data. Thin vectors and contours represent the 350 μm polarization and flux density. All vectors have been rotated 90° to show the direction of the inferred magnetic field. The hourglass field lines and circle with radius, R_{ridge} , equal to 0.1 pc (45") are the same as Fig. 4 (discussed in § 3.3.2).

TABLE 1
WAVELENGTH DEPENDENCE OF POLARIZATION

| Source | Wavelength (μm) | Beam (arcsec) | Polarization (%) | Position Angle (deg) |
|----------|------------------------------|---------------|------------------|----------------------|
| KL..... | 100 | 35 | 1.05 ± 0.03 | 31 ± 1 |
| | 350 | 18 | 1.4 ± 0.1 | 32 ± 2 |
| | 350 ^a | ~ 30 | 2.1 ± 0.3 | 31 ± 2 |
| | 1300 ^b | 30 | 2.7 ± 0.3 | 34 ± 3 |
| KHW..... | 100 ^c | ~ 60 | 1.5 ± 0.1 | 35 ± 2 |
| | 350 | 18 | 2.3 ± 0.4 | 27 ± 5 |
| | 350 ^d | ~ 30 | 2.4 ± 1 | 21 ± 10 |
| | 1300 ^b | 30 | 5.7 ± 1.3 | 42 ± 6 |

^a Stokes parameters from the five measurements nearest to KL are averaged.

^b Leach et al. 1991.

^c Stokes parameters from four measurements nearest to the 1300 μm pointing center are averaged.

^d Stokes parameters of the three nearest measurements to 1300 μm pointing center are averaged.

polarization at 100 and 350 μm . The lower mean and maximum percent polarization at 350 μm is therefore a result of the smaller spatial coverage and not intrinsic properties of the dust grains or the environment for grain alignment. At KL, 100, 350, and 1300 μm (Leach et al. 1991) position angles are all consistent with a value of 32° (see Table 1). Some previous measurements have discrepant values: as low as $16^\circ \pm 4^\circ$ (100 μm ; Gonatas et al. 1990) and as high as $44^\circ \pm 5^\circ$ (800 μm ; Flett & Murray 1991). However, from our data combined with 1300 μm data, we find no evidence for a shift in position angle with wavelength at KL.

At KL and KHW (exceptions to the above trend), we find that the percent polarization increases with wavelength (see Table 1). The polarization in KHW is discussed in § 3.2.2. Figure 10 shows polarization measurements for different wavelengths (smoothed to give similar resolutions of $\sim 30''$) at KL. In the limit of low optical depth, equation (1) simplifies to

$$P = \eta(1 - K\nu^\beta), \quad (2)$$

where we have written the optical depth as $\tau_\nu = K\nu^\beta$. Assuming $\beta = 1$, a linear fit to the KL data implies $\tau_{100} = 0.6$ and $\eta = 2.7\%$. Using $\beta = 2$, the fit implies $\tau_{100} = 0.6$ and $\eta = 2.5\%$; however, the fit does not well represent the

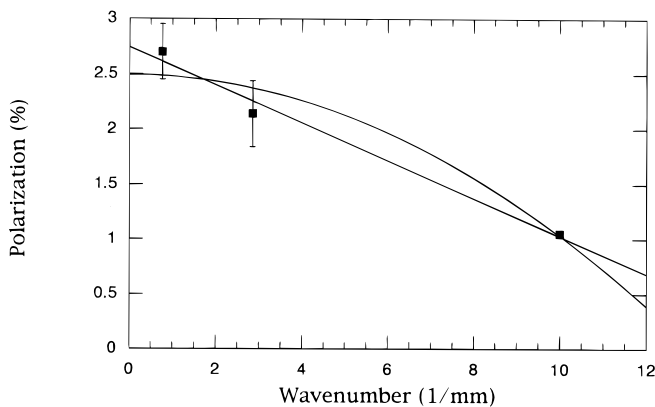


FIG. 10.—Polarization vs. wavenumber ($1/\text{mm}$). The polarization, averaged to a beam size of $\sim 30''$ (Table 1), decreases with wavenumber (increases with wavelength) at KL. The curves show fits to equation (2) with $\beta = 1$ ($\eta = 2.7\%$ and $\eta \times K = -0.17\% \text{ mm}$) and $\eta = 2$ ($\beta = 2.5\%$ and $\eta \times K = -0.014\% \text{ mm}^2$).

longer wavelength data. Wright et al. (1992) have modeled the photometric spectrum of the hot core associated with KL and find optical depths as high as $\tau_{1.1\text{mm}} \sim 0.5\text{--}0.9$ on small linear scales ($\sim 3''\text{--}8''$) with an emissivity dependence of $\beta = 2$. Far-infrared fluxes (50 and 100 μm) with lower resolution ($60''$) give an optical depth of 0.3 for a beam centered on KL (Werner 1982). Our radiative transfer model indicates that the intrinsic polarization at 100 μm in a $30''$ beam has been reduced from $\sim 2.7\%$ to 1% as the dust becomes opaque at shorter wavelengths. This opacity is due primarily to clumps well below our resolution. The intrinsic polarization of 2.7% is still below the polarization in extended regions (8%), and thus the opacity only gives a partial explanation to the radial decrease of polarization toward KL. Aitken et al. (1997) have used 12.5 and 17 μm polarimetry at arcsecond resolution to argue that field structure at smaller scales can account for the low polarization at KL. Although we see no evidence for variations in the position angles across the ridge (§ 3.3.2), we cannot rule out this interpretation.

3.2. Prominent Features

3.2.1. The BN/KL Region

Figure 11 shows prominent near-infrared, millimeter, and radio features in a $90''$ field surrounding the BN/KL region (hereafter BN/KL). The KL Nebula, located $10''$ south of the BN object (hereafter BN), collectively includes the near-infrared sources IRC2–5 (Genzel & Stutzki 1989) and dominates the flux for $\lambda > 30 \mu\text{m}$. At longer wavelengths it is apparent as the “hot core.” The large luminosity ($\sim 10^5 L_\odot$) in OMC-1 is thought to be due to young, high-mass stars in this region.

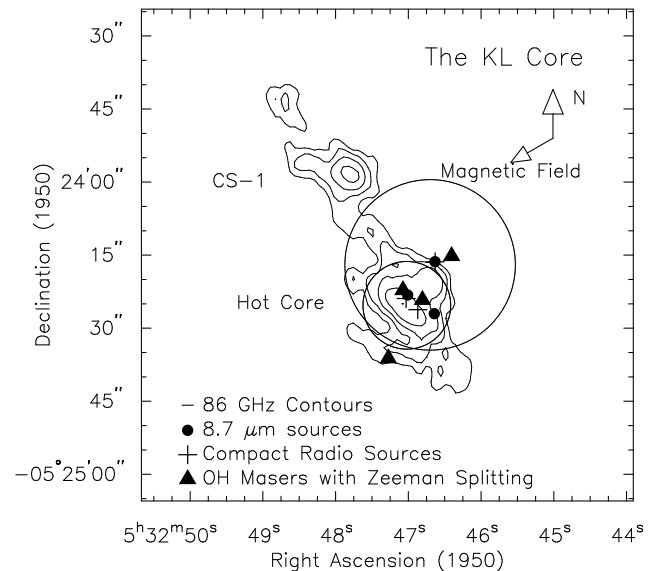


FIG. 11.—Prominent features in the KL core (§ 3.2.1). Contours show the 86 GHz continuum emission (Plambeck et al. 1995), with the CS-1 and hot core peaks labeled. Black dots represent infrared peaks at 8.7 μm (IRC1 [BN], IRC4, and IRC2, clockwise from north). Crosses represent radio point sources (coordinates taken from Gezari 1992). Filled triangles give the positions of the OH masers with Zeeman split lines (Heiles et al. 1993; Johnston, Migenes, & Norris 1989; discussed in § 4.1). Circles give the beam sizes and nominal pointing centers for the 100 μm ($35''$ beams) and 350 μm ($18''$ beams) observations. The region within the $18''$ circle is generally considered the KL nebula, south of BN and encompassing IRC2, IRC4, and the hot core. The mean magnetic field direction (120° ; § 3.3.1) is given relative to north.

Extensive spectropolarimetry has been carried out for the BN object (Chrysostomou et al. 1996; Lonsdale et al. 1980). Lee & Draine (1985) have modeled the polarization spectrum with combinations of “astronomical silicate” and “graphite” grains and find that near-infrared polarization at BN is due to dichroism and not scattering. At $2.2\ \mu\text{m}$, the polarization, P_{abs} (by absorption), is 18.4% with a position angle of 115° (Jones 1989; Lonsdale et al. 1980). This position angle is orthogonal to the polarization by emission, 32° . The optical depth at $2.2\ \mu\text{m}$ has been estimated from the $9.7\ \mu\text{m}$ silicate feature to be 11.0 (Jones 1989), which gives $P_{\text{abs}}/\tau = 1.7\%$. Comparison of the optical (P_{abs}) to far-infrared (P_{em}) measurements is given by $P_{\text{em}} = A(\lambda_1, \lambda_2)P_{\text{abs}}/\tau$, where $A(\lambda_1, \lambda_2)$ is the correction for change in dielectric function from the near- to the far-infrared (Hildebrand 1988). Using the apparent polarization (1.1%) at $100\ \mu\text{m}$, we derive $A = 0.6$; however, if we use the intrinsic polarization (2.7%; § 3.1.3), we derive $A = 1.6$. Hildebrand & Dragovan (1995b) compute $A = 1.7$ for astronomical silicate and $A = 1.1$ for graphite, for $\lambda_1 = 100\ \mu\text{m}$ and $\lambda_2 = 2.2\ \mu\text{m}$. Thus, the position angles and percent polarization are consistent with silicate grains that cause polarization by absorption in the near-infrared and polarization by emission in the far-infrared and submillimeter.

The hot core as well as the extended emission up to CS-1 ($45''$ northeast of the hot core) is elongated perpendicular to the magnetic field (see Fig. 11). However, the axis of the larger scale OMC-1 ridge is oriented more north-south (e.g., KHW is $90''$ south of KL; see Fig. 1). Velocity information is complicated by high-velocity outflows and multiple sources. We take a likely value of the line width to be $\sim 3\ \text{km s}^{-1}$ (FWHM) from maps of CS $J = 2-1$ (Mundy et al. 1988) and NH_3 (Batra et al. 1983). A velocity gradient extending across KL from the southwest ($\sim 7.5\ \text{km s}^{-1}$) to the northeast ($\sim 10\ \text{km s}^{-1}$) has been explained by two overlapping clouds (velocities of 8 and $10\ \text{km s}^{-1}$) or by Keplerian rotation along the ridge. Contours of constant radial velocity in CS (Mundy et al. 1988) show the steepest gradient at an angle 25° from north (i.e., approximately along the elongation from the hot core to CS-1). Regardless of the explanation, the velocity gradient implies an angular momentum axis at 115° from north, which is in good agreement with the inferred direction of the ambient magnetic field (120°). Two types of outflows originate near IRC2 (see Genzel & Stutzki 1989, and references therein). The low-velocity flow (expanding doughnut), traced by H_2O masers, is oriented at 45° along the hot core's elongation. The high-velocity flow (plateau), traced by CO emission, is oriented at 135° nearly parallel to the magnetic field orientation.

In summary, the 2.2 , 100 , and $350\ \mu\text{m}$ polarization measurements imply that silicate dust grains have been aligned by the magnetic field at an angle of 120° . This direction is (1) perpendicular to the elongation of the hot core, (2) perpendicular to the extended structure up to CS-1 but not as far as the OMC-1 ridge connecting to KHW, (3) parallel to the angular momentum axis, and (4) parallel to the high velocity molecular outflow from IRC2.

3.2.2. KHW (OMC-1S)

The KHW feature (Fig. 1) is prominent at $\lambda > 350\ \mu\text{m}$ (Keene, Hildebrand, & Whitcomb 1982). For $\lambda < 200\ \mu\text{m}$, it appears as an elongation of the OMC-1 ridge (Fig. 3) and shows no hint of structure in maps of color temperature ($50/100\ \mu\text{m}$) or $100\ \mu\text{m}$ optical depth ($60''$ resolution;

Werner 1982). While the mass of KHW ($50\ M_\odot$) is similar to KL, the dust temperature ($45\ \text{K}$) is lower than at KL ($70\ \text{K}$). The temperature difference is most likely due to the heating sources; KL is heated internally by sources near the hot core, while KHW is most likely heated externally by the Trapezium (see offset of $[\text{C II}]$ emission in Fig. 1). Since the $100\ \mu\text{m}$ emission shows only an extension of the OMC-1 ridge, it appears that the $100\ \mu\text{m}$ emission samples warmer dust on the edges of the KHW clump closer to the M42 H II cavity. At longer wavelengths ($\lambda > 200\ \mu\text{m}$), the emission is less sensitive to temperature and traces the high column density of the cold clump.

Comparisons of the polarization at $100\ \mu\text{m}$ (this work), $350\ \mu\text{m}$ (this work), and $1300\ \mu\text{m}$ (Leach et al. 1991) are confused by the location of the emitting dust, the effects of systematic errors (§ 2.1), and the lack of spatial coverage at 350 or $1300\ \mu\text{m}$. Despite these limitations, it is evident that the polarization at millimeter wavelengths is considerably higher than the polarization at far-infrared wavelengths (see Table 1). The position angles show slight ($1\ \sigma$) deviations between the 100 and $350\ \mu\text{m}$ measurements for the points between KHW and the Trapezium (see Fig. 9). At a position $45''$ northeast of KHW (between the Trapezium and the dense molecular material), spatially coincident measurements have position angles of $\phi_{100} = 28.1 \pm 0.3 \pm 1.3$ (statistical and systematic errors, respectively) and $\phi_{350} = 18.1 \pm 8.4 \pm 9.2$ (statistical and systematic, respectively). If future measurements find a significant variation in the angles, it might indicate that the magnetic field changes direction between the warm dust sampled near the H II interface and the colder dust deeper in the molecular cloud.

3.2.3. The Bar

The Orion bar has been described as an edge-on photo-dissociation region (PDR) (Tielens & Hollenbach 1985b), which shows a stratification of atomic and molecular gas and a gradient of warm to cool dust. This can be seen in the offset of $158\ \mu\text{m}$ $[\text{C II}]$ emission from $350\ \mu\text{m}$ dust emission (Fig. 1), which implies that the submillimeter dust samples a volume different from the H II/molecular interface.

Although systematic errors make the position angles uncertain in the bar (§ 2.1), our results show that the percent polarization is low compared to surrounding areas. In Figure 6c, we show a cut from KL through the bar. The normalized flux shows a secondary peak at the bar that is roughly 30% higher than the adjacent points. The polarization has minima at both KL and the bar and rises to a value of $\sim 4\%$ in the intervening material. The polarized flux shows a smooth distribution slowly decreasing away from KL (§ 3.1) and shows no deviation from this distribution across the bar. This implies that the far-infrared flux in the bar comes from two regions: the background molecular cloud contributes $\sim 70\%$ of the flux, which is polarized, and the bar contributes an additional 30% of flux, which is *unpolarized*. Thus, although both the bar and KL have minima of polarization, we can expect the reasons for the minima to be different.

Small opaque clumps in the bar that are below our resolution will reduce the observed polarization (§ 3.1.2). Tauber et al. (1994) estimate that a number (~ 10) of clumps ($n > 10^6\ \text{cm}^{-3}$; $R \sim 0.025\ \text{pc}$) may exist within the bar. Such clumps would have a column density of $7.5 \times 10^{22}\ \text{cm}^{-2}$ and a $100\ \mu\text{m}$ optical depth of 0.1. This optical depth is an order of magnitude below what is necessary to signifi-

cantly reduce the polarization. A second explanation considers the bar as a limb-brightened clump adjacent to the M42 H II region. If the magnetic field has been pushed out by the H II region, it will be oriented along the line of sight through the bar (see Fig. 2). Thus, we infer that the low polarization in the bar is due to a magnetic field that has been directed along the line of sight by the H II region.

3.2.4. The Dark Bay

Apparent in most optical pictures of the M42 nebula is a feature known as the dark bay, which extends across M42 from the northeast, partially extinguishing the nebula. There is a spatial correlation between the optical dark bay and a far-infrared feature roughly 2' east of KL ($\alpha \sim 5^{\text{h}}32^{\text{m}}57^{\text{s}}$; $\delta \sim -5^{\circ}24'20''$; see Figs. 1 and 3). The dark bay also correlates with H I absorption, which has been mapped with the 21 cm Zeeman effect to measure the line-of-sight magnetic field (Roberts, Crutcher, & Troland 1996; Troland, Heiles, & Goss 1989). The total column density of the velocity integrated H I line is $\sim 10^{21} \text{ cm}^{-2}$ (assuming $T_{\text{ex}} = 29 \text{ K}$), which corresponds a dust extinction of $A_V \sim 1$ (consistent with the optical extinction) and an optical depth of $\tau_{100} \sim 10^{-3}$. The $100 \mu\text{m}$ flux near the dark bay has an optical depth of $\tau_{100} \sim 10^{-2}$ (Werner 1982). However, the flux difference between the dark bay and surrounding areas is $\sim 10\%$ (see Fig. 3), which implies that the optical depth of the foreground dark bay itself is $\tau_{100} \sim 10^{-3}$, consistent with the optical extinction and H I absorption estimates.

The $100 \mu\text{m}$ polarization across the dark bay decreases from greater than 3% in surrounding areas to $\sim 2\%$ at the feature. However, while the polarization decreases

across the dark bay, the polarized flux remains nearly uniform, which implies that the flux from the dark bay is unpolarized. This is consistent with 90% of the emission coming from the background molecular cloud and 10% unpolarized emission coming from the foreground dark bay. As in the bar, we infer that the unpolarized emission in the foreground feature is due to the magnetic field pointing along the line of sight. If the foreground dust samples the same volume as the H I material, then our interpretation of a field inclination oriented near the line of sight is consistent with the conclusion of Troland et al. (1989).

3.3. The Distribution of Polarization Angles

3.3.1. The Mean Field

We define the “mean field” to be the magnetic field pervading the large-scale Orion A cloud. We define the “ambient field” to be the field in the ambient envelope, directly outside of the OMC-1 ridge (see Fig. 2); field lines in the ambient envelope connect to the field in the OMC-1 ridge. Because of Orion’s proximity, the extinction from the local ISM is low, and thus Orion allows reasonable comparisons between the polarization in optical, far-infrared, and submillimeter wavelengths. Measurements of optical polarization from starlight should be perpendicular to the far-infrared and submillimeter polarization by emission, if the measurements sample the same mean field.

Figure 12 shows histograms of the position angles for far-infrared and submillimeter measurements and for optical polarization measurements from stars in the nearby cloud, Lynds 1641, and for stars near the Orion Nebula.

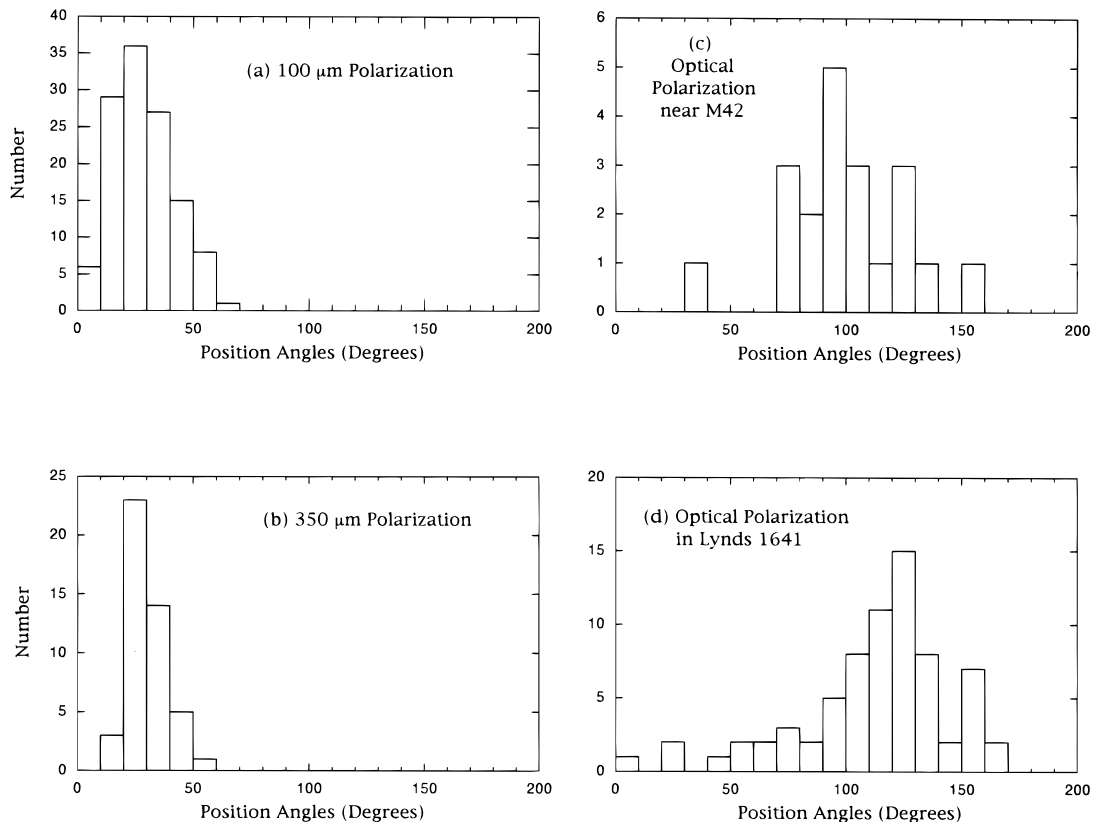


FIG. 12.—Histograms of $100 \mu\text{m}$, $350 \mu\text{m}$, and optical polarization angles: (a) $100 \mu\text{m}$ polarization angles; (b) $350 \mu\text{m}$ polarization angles; (c) optical polarization of starlight near the Orion nebula (Breger 1976); (d) optical polarization for stars behind the nearby giant molecular cloud, Lynds 1641 (Vrba et al. 1988). The far-infrared, submillimeter, and optical polarization measurements are all consistent with a mean field in the plane of the sky at an angle of 120° (east of north).

The 100 and 350 μm position angles both have a mean value of 29° and have dispersions of 13° and 8° , respectively. We attribute the 100 μm dispersion, which is greater than the mean errors (1.5 statistical; 5.6 systematic), to be due to the large-scale distortion of the magnetic field (§ 3.3.2). The 350 μm dispersion, which is slightly larger than the errors (5.7 statistical), is also attributed to the distortion at the edge of the region covered.

Vrba, Strom, & Strom (1988) surveyed the optical polarization of 219 stars in the giant molecular cloud, Lynds 1641. This cloud ($1^\circ \times 4^\circ$) extends southeast from M42 at angle of 145° and has a mass derived from low-resolution CO maps of $2 \times 10^5 M_\odot$. The polarization of the stars with $P < 1\%$ is thought to sample the interstellar medium to the cloud. For these stars, the polarizations are clustered around $P = 0.25\%$ and $\phi = 40^\circ$, which we take to be the ISM polarization. The polarization of the remaining 71 stars with $P > 1\%$ is thought to be due primarily to the molecular cloud. The polarization results for these stars have been corrected for the ISM polarization and have a mean position angle of 112° . This average angle is consistent with a magnetic field at 120° . On this large scale, the field is 35° from the long axis of the cloud.

On a smaller scale surrounding the dense M42 region, Breger (1976) has measured the polarization of some 200 stars in a 2.5×2.5 region. In an analysis similar to that of Novak et al. (1989), we have not considered the results for stars with $P < 1.5\%$ (6 times the local ISM value), stars thought to be shell stars (Breger 1977), or stars with abnormal $P(\lambda)$ dependencies (Breger, Gehrz, & Hackwell 1981). The remaining 20 stars are good candidates to contain only polarization by absorption of the molecular cloud surrounding M42. The polarization angles for this small sample of stars have a mean value of 100° .

Combining the results of optical, far-infrared, and sub-millimeter polarization, the mean field through OMC-1 is at an angle of $\sim 120^\circ$. This result is consistent with a 90° change in angle between polarization by emission and absorption. We assume that the ambient field in the envelope surrounding OMC-1 is uniform and is parallel to the mean field.

3.3.2. The Magnetic Distortion

The maps of magnetic field vectors (Figs. 4 and 9) imply a large-scale distortion of the magnetic field. To aid in describing the field distortion, we define a coordinate system, (ρ, z) , oriented parallel to the ambient field (120°) and centered at the position of KL ($\rho = z = 0$).

Extreme deviations from the ambient field have a negative deflection (difference from the nominal 30° polarization angle) of -30° at $Z \sim -80''$ and $\rho \sim +90''$ and a positive deflection of $+25^\circ$ at $Z \sim +100''$ and $\rho \sim +90''$. We therefore take the nominal field distortion to be $\sim 25^\circ$ at a characteristic scale of $120''$ (0.3 pc). The radius of curvature of this distortion is $\sim 240''$ (0.5 pc). On the eastern edge of the map, the vectors are at an angle of $\sim 120^\circ$ and appear to be beyond the distortion. This is consistent with field lines connecting to a uniform ambient field beyond a scale of $R_{\text{pinch}} \sim 240''$ (0.5 pc).

In Figures 4 and 9, we have sketched field lines through the vectors assuming that they connect to a large-scale field that is uniform at an angle of 120° (§ 3.3.1). These lines describe a magnetic field that (1) is symmetric about a point (asterisk) $45''$ southwest of KL, (2) is uniform across the

ridge ($R_{\text{ridge}} < 45''$ from the symmetry point) with no local distortions around KL or KHW, (3) has a symmetrical distortion at intermediate scales ($45'' < R < 240''$) with a deflection of $\sim 25^\circ$, and (4) connects to the ambient field at scales greater than $R_{\text{pinch}} = 240''$ (0.5 pc).

4. DISCUSSION

Figure 2 presents our schematic picture of the magnetic field threading through OMC-1. According to this interpretation, the large-scale field is uniform (§ 3.3.1). In the background molecular cloud, the field has been distorted at scales less than $R_{\text{pinch}} \sim 0.5$ pc from the ridge (§ 3.3.2). Below, we argue that the OMC-1 ridge has gravitationally pulled the magnetic field into an hourglass shape. Around M42, we argue that the low polarization in the bar and dark bay is due to a field that has been expelled from the H II region.

4.1. The OMC-1 Environment

Consider two regions that have independent measurements of the magnetic field strength: the foreground H I envelope and the KL core on OMC-1 ridge. Maps of H I absorption at $18''$ resolution have shown two velocity components associated with the material in the foreground of Orion A (Van der Werf & Goss 1989). In the high-velocity component (6 km s^{-1}), Zeeman observations give values for the magnetic field along the line of sight of -40 to $-100 \mu\text{G}$ (toward the observer), while the results on the lower velocity component (4 km s^{-1}) have low statistical significance (Troland et al. 1989; Roberts et al. 1996). We have defined the ambient envelope (§ 3.3.1) to be the region outside of the OMC-1 ridge (*dashed region*, Fig. 2) and assume that the magnetic field is uniform and inclined to the line of sight at an angle γ . Assuming that the line-of-sight component of the ambient field is similar to the foreground H I envelope, we write the total field strength in the ambient envelope as

$$B_{\text{ambient}} = -70 \left[\frac{f}{\cos(\gamma)} \right] \mu\text{G}, \quad (3)$$

where f is an unknown conversion factor between the H I envelope and the ambient material and $-70 \mu\text{G}$ is an average value of the line-of-sight field in the H I envelope. With the values of f and γ unknown, we adopt a value of $-100 \mu\text{G}$ for the total field strength and use the density (400 cm^{-3}) and line width (3 km s^{-1}) associated with the H I envelope to represent the conditions in the ambient envelope (listed in Table 2).

The KL and KHW clumps are dense cores on the OMC-1 ridge. The magnetic field strength has been measured for H₂O and OH masers (Heiles et al. 1993, and references therein). The OH masers sample lower densities (10^7 cm^{-3}) than the H₂O masers (10^9 cm^{-3}) and therefore are more likely to sample the same magnetic field as our measurements. The collection of OH masers with Zeeman split lines (Fig. 11) have total field strengths that range from -0.8 to -2.0 mG (Heiles et al. 1993; Johnston, Migenes, & Norris 1989). We take a most likely value of -1 mG to represent the total magnetic field strength in the KL core. The 350 μm polarization on the ridge is characterized by polarized flux that increases into the ridge (§ 3.1) and position angles that are uniform across the ridge (scales less than 0.1 pc; § 3.3.2); on these scales, we see no evidence of

TABLE 2
CLOUD PARAMETERS

| Name | ΔV (km s ⁻¹) | σ (km s ⁻¹) | σ_T (km s ⁻¹) | σ_{NT} (km s ⁻¹) | Density (cm ⁻³) | Magnetic Field (μ G) | Radius (pc) |
|-----------------------|-------------------------------------|-----------------------------------|-------------------------------------|--|--------------------------------|------------------------------|----------------|
| Ridge cores | 3 ^a | 1.3 | 0.1 | 1.3 | 10 ⁶ | 1000 ^b | 0.04 |
| Ambient envelope..... | 3 ^c | 1.3 | 0.49 | 1.2 | 400 ^c | 100 ^c | 0.6 |

^a CS $J = 2-1$; Mundy et al. 1988.

^b OH masers; Heiles et al. 1993.

^c H I; Troland et al. 1989.

magnetic structure resulting from local pinching around the KL or KHW cores or field variations due to Alfvén waves (§ 4.3). Because of the uniformity of the 350 μ m polarization measurements, we infer that the magnetic field is uniform across the ridge with a strength of -1 mG.

4.2. An Hourglass Magnetic Field?

We propose that the pinch structure in the magnetic field is due to a gravitational distortion by the OMC-1 ridge. This inference is supported by the following: (1) greater than 70% of the flux is from the background molecular material behind the H II region, (2) the symmetry of the vectors show structure that is pulled into the OMC-1 ridge rather than away from the H II region, and (3) the distortion is centered on the ridge and not the center of the H II region (i.e., the Trapezium). This model also connects independent measurements of the magnetic field on the ridge and ambient envelope and is consistent with the gravitational force balancing the magnetic tension.

4.2.1. Magnetic Flux Compression

Heiles et al. (1993) have estimated the magnetic flux at two size scales on the order of the ridge cores and ambient envelope. They find equal magnetic fluxes at these widely different size scales. Using the hourglass morphology of the magnetic field, we compare the magnetic field strength in the ambient envelope with that in the ridge cores. Assuming a cylindrical geometry, the field lines (sketched in Fig. 4) define magnetic flux tubes tracing from the ambient envelope into the ridge. The magnetic flux in the ambient envelope is given by $\Phi = B_{\text{ambient}} \pi R^2$, where R is the radius of a magnetic flux tube. On the ridge the uniform field lines give a magnetic flux, Φ , equal to $B_{\text{ridge}} \pi r^2$, where r is the radius of a flux tube on the ridge. For a given flux tube, $B_{\text{ridge}} = C \cdot B_{\text{ambient}}$, where we have defined a magnetic compression factor, C , to be equal to $(R/r)^2$. The field lines sketched in Figure 4 are uniform on the ridge and envelope and have a factor of 2 closer spacing on the ridge, which corresponds to a magnetic compression of $C = 4$. This compression estimate does not account for an hourglass tilted to the line of sight or for averaging the field through the optically thin cloud. Since both of these effects act to increase the field compression, we consider $C = 4$ to be a lower limit. Applying this compression to the ambient field ($B_{\text{ambient}} = -100$ μ G), we derive a field strength on the ridge of

$$B_{\text{compressed}} = -0.3 \left(\frac{C}{4} \right) \left[\frac{f}{\cos(\gamma)} \right] \text{ mG}. \quad (4)$$

For reasonable estimates of $f/\cos(\gamma)$ and/or with increased field compression, the hourglass description gives a field strength on the ridge of order -1 mG, which is consistent with the measurements of OH masers in the KL core. Thus,

the hourglass morphology of the magnetic field can qualitatively link two independent measurements of the magnetic field strength.

4.2.2. Magnetic Tension

Assuming that the magnetic field has been pulled into an hourglass shape by gravity, we compare the magnetic tension to the gravitational force. Consider a region 0.1 pc northeast of KL, where the field has a radius of curvature of ~ 0.5 pc. The tension $[(1/4\pi)(\mathbf{B} \cdot \Delta)\mathbf{B}]$, approximated as $(1/4\pi)B^2/R$, is given by

$$f_{\text{tension}} = 5 \times 10^{-26} \left(\frac{B}{1 \text{ mG}} \right)^2 \left(\frac{0.5 \text{ pc}}{R} \right) \text{ dyn cm}^{-3}, \quad (5)$$

and the gravitational force ($GM\rho/D^2$) is given by

$$f_{\text{gravity}} = 5 \times 10^{-26} \left(\frac{M}{100 M_{\odot}} \right) \left(\frac{n}{10^5 \text{ cm}^{-3}} \right) \times \left(\frac{0.1 \text{ pc}}{D} \right)^2 \text{ dyn cm}^{-3}. \quad (6)$$

With these estimates of the field strength and curvature, mass, and density, the gravitational force density is sufficient to distort the magnetic field, until it is held by magnetic tension.

4.2.3. H II Distortion

The magnetic field, interacting with the M42 nebula, is likely to be pushed out by the ionized H II region, as shown schematically in Figure 2. This has been argued in general for H II regions interacting with molecular clouds (Kannappan & Goodman 1998). For example, in M17 the H II region is edge-on to the molecular material, and the polarization vectors show circular structure around the nebula (Dotson 1996). This configuration has been interpreted as a magnetic field that has bulged around the H II region. In contrast to M17, the M42 nebula has blistered in front of the Orion molecular cloud. As a natural consequence of this geometry, limb-brightened clumps around the H II region are threaded by a magnetic field that is projected along the line of sight (see Fig. 2). A magnetic field oriented along the line of sight causes unpolarized emission. We attribute the low polarization in the bar (§ 3.2.3) and dark bay (§ 3.2.4) to this effect. However, we have argued that less than 30% of the flux is due to these foreground features; most of the emission comes from the background molecular cloud behind the H II region. The symmetry of the polarization vectors in the background molecular material does not show circular structure around the H II region, as in M17; rather, the field appears to be pulled into the OMC-1 ridge.

4.3. Scales of Magnetic Structure

Mouschovias (1991) considered three natural length scales appropriate for molecular clouds: the critical magnetic length scale (λ_M), the minimum Alfvén length scale (λ_A), and the thermal (Jeans) length scale (λ_T). The non-thermal line widths in OMC-1 suggest a nonthermal (Jeans) length scale (λ_{NT}). For parameters appropriate to the envelope of OMC-1, these scales are given by

$$\lambda_M = 7.6 \left(\frac{B}{100 \mu\text{G}} \right) \left(\frac{400 \text{ cm}^{-3}}{n} \right) \text{ pc}, \quad (7)$$

$$\lambda_A = 2.4 \left(\frac{B}{100 \mu\text{G}} \right) \left(\frac{400 \text{ cm}^{-3}}{n} \right) \left(\frac{3 \times 10^{-3} \text{ cm}^{-3}}{K} \right) \text{ pc}, \quad (8)$$

$$\lambda_T = 0.8 \left(\frac{T}{29\text{K}} \right)^{1/2} \left(\frac{400 \text{ cm}^{-3}}{n} \right)^{1/2} \text{ pc}, \quad (9)$$

and

$$\lambda_{NT} = 2.3 \left(\frac{\sigma}{1.2 \text{ km s}^{-1}} \right) \left(\frac{400 \text{ cm}^{-3}}{n} \right)^{1/2} \text{ pc}, \quad (10)$$

where B is the magnetic field strength, n is the density, K is the ionization parameter for ionization driven by cosmic rays, T is the temperature, and σ is the dispersion of the molecular line width. For parameters characteristic of the ridge cores (see Table 2), these scales correspond to $\lambda_M = 0.03$ pc, $\lambda_A = 0.01$ pc, $\lambda_T = 0.03$ pc, and $\lambda_{NT} = 0.05$ pc.

The magnetic and Jeans lengths are the scales at which gravity is balanced by magnetic and kinetic pressures, respectively. Using the parameters characteristic of the ambient envelope, both the magnetic and Jeans length scales are greater than the scale of magnetic structure observed in OMC-1 ($R_{\text{pinch}} = 0.5$ pc). While it is possible that such structure may exist on scales much larger than the mapped region in Orion, we give two arguments against this interpretation. First, hourglass structures are not seen in M17 (Dotson 1996) or other high-mass star-forming regions mapped with far-infrared polarimetry (Hildebrand et al. 1995). Since these objects are at greater distances than OMC-1, the measurements are sensitive to linear scales much larger than ~ 0.5 pc. Second, the vectors on the eastern edge of our map are at $\sim 120^\circ$, which implies that the field has connected to the mean field and that our map samples to the edge of the hourglass structure (discussed in § 3.3.2). Thus, the observed magnetic structure appears to have a radius (0.5 pc) that is less than the Jeans scale and an order of magnitude less than the magnetically critical scale.

Alfvén waves could provide support of cloud cores and explain the observed nonthermal line widths. Although the polarization shows no significant dispersion in the position angles on the ridge, waves averaged along the line of sight could act to reduce the polarization while giving uniform position angles. However, waves with a frequency higher than the neutral-ion collision rate will be rapidly damped, as the ions decouple from the neutrals. Thus, Alfvén waves will only be supported above the minimum Alfvén wavelength (λ_A). For the core, this scale corresponds to $4''.6$, which is smaller than our highest resolution.

The observed uniformity in position angles could be due to averaging over many waves along the line of sight in an optically thin cloud. The size of the cloud along the line of sight is estimated to be $Z_{\text{cloud}} = N_H/n$, where N_H is the column density. The number of waves possible along the

line of sight is given by the ratio

$$\frac{Z_{\text{cloud}}}{\lambda_A} = 10 \left(\frac{K}{3 \times 10^{-3} \text{ cm}^{-3}} \right) \left(\frac{1 \text{ mG}}{B} \right) \left(\frac{\tau_{100 \mu\text{m}}}{0.3} \right), \quad (11)$$

where the column density has been converted to a $100 \mu\text{m}$ optical depth (Hildebrand 1983). Along the ridge, the optical depth approaches unity and our beams average over many possible Alfvén wavelengths. Off the OMC-1 ridge, the density and field strengths are likely to be reduced. Assuming a density of $4 \times 10^3 \text{ cm}^{-3}$, field strength of $100 \mu\text{G}$, and $\tau_{100 \mu\text{m}} = 0.03$, the minimum Alfvén wavelength and number of cells are $\lambda_A = 110''$ and $Z_{\text{cloud}}/\lambda_{\text{min}} = 10$, respectively. In this more diffuse region of the cloud, our measurements could spatially resolve Alfvén wave variations; however, the measurements are still averaging over a number of possible Alfvén wavelength cells. For these reasons, we regard the Chandrasekhar & Fermi (1953) relation, estimating the field strength from the dispersion in line width and polarization angles, as inappropriate for our measurements.

4.4. Energy Arguments

For the parameters estimated for the ambient envelope and the ridge cores in OMC-1 (Table 2), we calculate the energy terms in the virial equation (McKee et al. 1993, and references therein). We assume a spherical clump threaded by a uniform magnetic field. Neglecting surface and time-dependent terms, the magnetic ($M \sim 1/6 B^2 R^3$), non-thermal kinetic ($K_{NT} \sim 3/2 M \sigma_{NT}^2$), thermal kinetic ($K_T \sim 3/2 M \sigma_T^2$), and gravitational ($W \sim -3/5 GM^2/R$) energies in the ambient envelope are given by

$$M = 10^{46} \left(\frac{B}{100 \mu\text{G}} \right)^2 \left(\frac{R}{0.6 \text{ pc}} \right)^3 \text{ ergs}, \quad (12)$$

$$K_{NT} = 10^{45} \left(\frac{n}{400 \text{ cm}^{-3}} \right) \left(\frac{\sigma}{1.2 \text{ km s}^{-1}} \right)^2 \left(\frac{R}{0.6 \text{ pc}} \right)^3 \text{ ergs}, \quad (13)$$

$$K_T = 10^{44} \left(\frac{n}{400 \text{ cm}^{-3}} \right) \left(\frac{\sigma}{0.5 \text{ km s}^{-1}} \right)^2 \left(\frac{R}{0.6 \text{ pc}} \right)^3 \text{ ergs}, \quad (14)$$

$$W = -10^{43} \left(\frac{n}{400 \text{ cm}^{-3}} \right)^2 \left(\frac{R}{0.6 \text{ pc}} \right)^5 \text{ ergs}, \quad (15)$$

where B is the magnetic field strength, n is the density, and σ is the dispersion in a region of radius R . Since these calculations assume a simple geometry and neglect important terms (surface terms), they merely show order-of-magnitude relationships between the energies.

The ambient envelope is dominated by the magnetic energy, where $M > K_{NT} > K_T > |W|$. Troland et al. (1989) have also estimated the energies in the H I envelope, using a cylindrical (rather than spherical) geometry and similar cloud parameters. They find similar qualitative results, namely that the magnetic energy is more than 2 orders of magnitude greater than the gravitational energy. Since the envelope is magnetically dominated, perhaps external pressure confines the region. In contrast, the energies on the OMC-1 ridge (parameters given in Table 2) give rough equipartition between the magnetic, kinetic (nonthermal),

and gravitational energies ($M \sim K_{\text{NT}} \sim |W| \sim 5 \times 10^{44}$ ergs), which are greater than the thermal kinetic energy ($K_T \sim 5 \times 10^{42}$ ergs).

4.5. A Model For Magnetically Regulated Star Formation

If one accepts the hourglass connection between the OMC-1 ridge and ambient envelope presented in § 4.2, one is faced with an envelope that is characterized by length scales far in excess of those measured by our observations (§ 4.3) and strongly supported by the magnetic field (§ 4.4). How then could the OMC-1 ridge and therefore stars have formed?

Consider two explanations. (1) External pressure (e.g., expansion of the M42 H II region) has compressed the molecular material and deformed the magnetic field lines. (2) Gravitational collapse, regulated by the magnetic field, has formed the OMC-1 ridge, pulling the field into an hourglass shape. We have argued that, while the low polarization in the bar can be explained by the expansion of the H II region pushing the field along the line of sight, the symmetry of the vectors in the background molecular cloud appear more likely to be pulled into the ridge than pushed out by the H II region. We therefore favor the gravitational explanation.

To account for the energy and length scale discrepancies, we consider an evolution based on the process of ambipolar diffusion. At scales above λ_J and below λ_A , neutrals slip with respect to magnetically tied ions, qualitatively increasing the density while maintaining a constant magnetic field strength. The increased density can have three effects on the dynamics of the cloud. First, the gravitational energy increases compared to the kinetic and magnetic energy. Second, the increased density will decrease the Alfvén velocity, which, if related to the nonthermal line widths, will decrease the kinetic energy to nearly thermal values. Third, the increased density will decrease the ionization fraction, which will steadily reduce the importance of the magnetic field.

Starting with the parameters characterizing the ambient envelope, we allow the density to increase until the magnetic and gravitational energies become equal. For the ambient envelope, this occurs at a density of 7000 cm^{-3} . By construction, the magnetic and gravitational energies are equal, but they are also within an order of magnitude of the kinetic energy. This critical envelope is characterized by length scales of $\lambda_M = 0.4 \text{ pc}$, $\lambda_T = 0.2 \text{ pc}$, and $\lambda_{\text{NT}} = 0.5 \text{ pc}$, which are all close to the observed length scale of 0.5 pc . Thus, once a region within the magnetically dominated cloud reaches equipartition between magnetic, kinetic, and gravitational energies, the length scales describing the collapse are consistent with the length scales of the observed hourglass field.

Another way to view the same process is to consider a magnetically supported cloud that forms a core by drawing mass from the surrounding envelope. Eventually the core collapses gravitationally, leaving behind a magnetically dominated envelope. We review the assumptions and observational evidence that led to this conclusion. (1) We assume that the parameters in the H I envelope adequately describe the ambient envelope surrounding the OMC-1 ridge. (2) We observe uniform polarization vectors on the ridge (Fig. 9) and infer a uniform magnetic field with a strength given by measurements of OH masers. (3) We observe an hourglass shape at a scale of 0.5 pc and infer that

it is the result of gravitational collapse. (4) Assuming that the magnetic, kinetic, and gravitational energies came into equipartition due to an ambipolar diffusion mechanism, we find agreement between the observed and calculated length scales of structure. Following this chain of arguments, we form a picture of a magnetically supported cloud that evolved by ambipolar diffusion into a state of equipartition, followed by collapse that formed the OMC-1 ridge and the high-mass stars in the BN/KL region.

The hourglass field is also characterized by (1) uniformity on smaller scales (straight field lines) and (2) a centroid that is between KL and KHW on the OMC-1 ridge. The uniformity of the field at scales less than 0.1 pc ($n = 10^5\text{--}10^6 \text{ cm}^{-3}$) may be an effect of averaging field structure through the cloud (§ 4.3). However, we find no evidence for local pinching of the magnetic field around the KL or KHW cores. To explain these field characteristics, we speculate that the field decoupled from the material at relatively low densities. However, the mean field is at an angle of 120° , which is parallel to the high-velocity outflow axis and the angular momentum axis of KL and is perpendicular to the elongation of the KL core. The agreement between these orientations is inconsistent with our speculation that the field decoupled from the material at these scales. In contrast, the larger scale elongation of OMC-1, from KHW up the OMC-1 ridge to OMC-2, is oriented north-south (0°) and the cloud, Lynds 1641 (§ 3.3.1), is oriented at 145° ; both of these large-scale elongations are neither parallel nor perpendicular to the magnetic field direction. Why then are the small-scale features oriented parallel to the magnetic field, while large-scale structures are seemingly unrelated to the magnetic field?

5. CONCLUSIONS

We summarize the conclusions of this paper in three categories: empirical trends in the data, observed and inferred properties of the magnetic field, and speculation into the evolution of high-mass stars.

5.1. Empirical Properties of the Polarization

1. Our data set for OMC-1 consists of 92 (independent) and 32 (oversampled) detections at $100 \text{ } \mu\text{m}$ and 46 (independent) detections at $350 \text{ } \mu\text{m}$, all with greater than 3σ statistical and systematic significance. For the $100 \text{ } \mu\text{m}$ data, the polarization ranges from 0% – 8% , and the median value is 4.2% . At $350 \text{ } \mu\text{m}$, the lower median value, 3.2% , is due to smaller spatial coverage.

2. Positions of reduced polarization correlate with intensity peaks across the map (KL, KHW, the bar, and the dark bay). This correlation is well described by high polarization in extended regions and a radial decrease in polarization toward KL. Although the percent polarization is reduced, the polarized flux increases into the OMC-1 ridge, which indicates that the grains in this dense region are elongated and aligned by the magnetic field.

3. The maximum polarization decreases with increasing optical depth and temperature, which both increase radially toward KL. For all positions with overlapping polarization and temperature measurements, the ratio T_{ex}/T_D is less than 2.

4. The polarization is constant with wavelength (far-infrared to submillimeter) over most of the OMC-1 ridge, except at KL and KHW, where the polarization increases with wavelength. At KL, the polarization spectrum fits a

radiative transfer model that implies a $100\ \mu\text{m}$ optical depth of 0.6 in a $\sim 30''$ beam and an intrinsic polarization of 2.7%.

5. At BN/KL, the polarization by emission (KL) is perpendicular to the polarization by absorption (BN). The ratio of percent polarization by emission to percent polarization by absorption per optical depth is 1.6, which is consistent with the computed value for silicate grains.

5.2. Observed and Inferred Properties of the Magnetic Field

1. Optical polarimetry (absorption) and far-infrared and submillimeter polarimetry (emission) show a mean magnetic field that is at $\sim 120^\circ$, pervading the giant molecular cloud from scales of 30 pc (Lynds 1641) to the extent of our $100\ \mu\text{m}$ map (1 pc) to the highest resolution of our submillimeter map (0.04 pc).

2. Within OMC-1, the polarization map shows a pinch, which we interpret to be an hourglass distortion of the magnetic field due to gravitational collapse. The distortion is centered at a point $45''$ southwest of KL along the OMC-1 ridge and extends to a radius, R_{pinch} , equal to 0.5 pc. The hourglass compression of the field is consistent with independent measurements of the field strength in the core and envelope. The curvature of the field is consistent with magnetic tension balancing the gravitational force of the OMC-1 ridge.

3. The polarization in the bar and the dark bay is low, which we attribute to a field that is directed along the line of sight by the M42 H II region.

4. At scales less than $R_{\text{ridge}} < 0.1$ pc, the polarization vectors are consistent with a uniform field. We find no evidence for distortion of the field due to a disordered component of the magnetic field. However, along the OMC-1 ridge, Alfvén waves could be maintained below our resolution, and our measurements, which sample the extent of the cloud, could average over many Alfvén wavelengths.

5.3. Speculation Into Magnetically Regulated Star Formation

1. From energy arguments, we find that the magnetic, kinetic, and gravitational energies are in rough equi-

partition in the KL core, while the magnetic energy is dominant in the ambient envelope.

2. The observed length scale for hourglass structure of the magnetic field ($R_{\text{pinch}} = 0.5$ pc) is smaller than the estimated magnetic or Jeans length scales in the ambient envelope. However, a critical envelope with higher density would give equipartition between the magnetic, kinetic, and gravitational energies and lengths scales of $\lambda_J \sim \lambda_M \sim 0.5$ pc.

3. Combining the above points, we offer a possible evolution for the structure in OMC-1. A molecular cloud supported by the magnetic field evolved by ambipolar diffusion, until the increased density gave rough equipartition between the magnetic, kinetic, and gravitational energies. Gravitational collapse ensued, pulling the magnetic field into an hourglass shape and leaving behind a magnetically dominated envelope. Cores on the ridge (i.e., KL) then collapsed supercritically to form high-mass stars.

I am grateful to my advisor, Roger Hildebrand, for giving me the opportunity, support, and guidance to do this research project. I am also grateful to his current and former students, C. D. Dowell, J. L. Dotson, S. R. Platt, G. Novak, J. A. Davidson, and M. Dragovan for advice and lively discussions on topics ranging from instrumentation to systematic effects to magnetic fields to surfing the big waves. I thank R. L. Akeson, J. E. Carlstrom, G. E. Ciolek, A. A. Goodman, D. A. Harper, S. J. Kannappan, A. Königl, P. Palmer, R. Rosner, and the referee for useful discussions and comments. I thank S. Knudsen, R. F. Loewenstein, T. McMahon, R. Pernic, D. Pernic, C. Wirth, and the staff of the Kuiper Airborne Observatory and Caltech Submillimeter Observatory for help preparing the instrument and for assistance during the observations. The instrumentation development and observations were supported by NASA grant NSG-2057 and NSF grant AST 89-17950. The CSO is funded by the NSF through contract AST 96-15025. I am grateful for support from the NASA graduate student research program, grant NGT 51311.

REFERENCES

- Aitken, D. K., Smith, C. H., Moore, T. J. T., Roche, P. F., Fujiyoshi, T., & Wright, C. M. 1997, *MNRAS*, 286, 85
- Batrla, W., Wilson, T. L., Bastien, P., & Ruf, K. 1983, *A&A*, 128, 279
- Bergin, E. A., Goldsmith, P. F., Snell, R. L., & Ungerechts, H. 1994, *ApJ*, 431, 674
- Breger, M. 1976, *ApJ*, 204, 789
- . 1977, *ApJ*, 215, 119
- Breger, M., Gehrz, R. D., & Hackwell, J. A. 1981, *ApJ*, 248, 963
- Chandrasekhar, S., & Fermi, E. 1953, *ApJ*, 118, 113
- Chrysostomou, A., Hough, J. H., Messinger, D. W., Whittet, D. C. B., Aitken, D. K., & Roche, P. F. 1996, in *ASP Conf. Proc. 97, Polarimetry of the Interstellar Medium*, ed. W. G. Roberge & D. C. B. Whittet (San Francisco: ASP), 243
- Crutcher, R. M., Mouschovias, T. C., Troland, T. H., & Ciolek, G. E. 1994, *ApJ*, 427, 839
- Cudlip, W., Furniss, I., King, K. J., & Jennings, R. E. 1982, *MNRAS*, 200, 1169
- Davis, L. D., & Greenstein, J. L. 1951, *ApJ*, 114, 206
- Dotson, J. L. 1996, *ApJ*, 470, 566
- Dotson, J. L., Dowell, C. D., Schleuning, D. A., & Hildebrand, R. H. 1998, in preparation
- Dragovan, M. 1986, *ApJ*, 308, 270
- Flett, A. M., & Murray, A. G. 1991, *MNRAS*, 249, 4P
- Genzel, R., & Stutzki, J. 1989, *ARA&A*, 27, 41
- Gezari, D. Y. 1992, *ApJ*, 396, L43
- Gonatas, D. P., et al. 1990, *ApJ*, 357, 132
- Gull, G. E., Houck, J. R., McCarthy, J. F., Forrest, W. J., & Harwit, M. 1978, *AJ*, 83, 1440
- Harper, D. A. 1974, *ApJ*, 192, 557
- Heiles, C., Goodman, A. A., McKee, C. F., & Zweibel, E. G. 1993, in *Protostars & Planets III*, ed. E. H. Levy & J. I. Lunine (Tucson: Univ. of Arizona Press), 279
- Hildebrand, R. H. 1983, *QJRAS*, 24, 267
- . 1988, *QJRAS*, 29, 327
- Hildebrand, R. H., Dotson, J. L., Dowell, C. D., Platt, S. R., Schleuning, D., Davidson, J. A., & Novak, G. 1995, in *ASP Conf. Proc. 73, Proc. of the Airborne Astronomy Symp. on the Galactic Ecosystem: From Gas to Stars to Dust*, ed. M. R. Haas, J. A. Davidson, & E. F. Erickson (San Francisco: ASP), 97
- Hildebrand, R. H., & Dragovan, M. 1995, *ApJ*, 450, 663
- Hildebrand, R. H., Dragovan, M., & Novak, G. 1984, *ApJ*, 284, L51
- Johnston, K. J., Migenes, V., & Norris, R. P. 1989, *ApJ*, 341, 847
- Johnston, K. J., Palmer, P., Wilson, T. L., & Bieging, J. H. 1983, *ApJ*, 271, L89
- Jones, T. J. 1989, *ApJ*, 346, 728
- Kannappan, S., & Goodman, A. A. 1998, in preparation
- Keene, J., Hildebrand, R. H., & Whitcomb, S. E. 1982, *ApJ*, 252, L11
- Leach, R. W., Clemens, D. P., Kane, B. D., & Barvainis, R. 1991, *ApJ*, 370, 257
- Lee, H. M., & Draine, B. T. 1985, *ApJ*, 290, 211
- Lonsdale, C. J., Dyck, H. M., Capps, R. W., & Wolstencroft, R. D. 1980, *ApJ*, 238, L31
- McKee, C. F., Zweibel, E. G., Goodman, A. A., & Heiles, C. 1993, in *Protostars & Planets III*, ed. E. H. Levy & J. I. Lunine (Tucson: Univ. of Arizona Press), 327
- Mouschovias, T. C. 1991, *ApJ*, 373, 169

- Mouschovias, T. C. 1995, in ASP Conf. Proc. 80, The Physics of the Interstellar Medium and the Intergalactic Medium, ed. A. Ferrara, C. Heiles, C. F., McKee, & P. Shapiro (San Francisco: ASP), 184
- Mundy, L. G., Cornwell, T. J., Masson, C. R., Scoville, N. Z., Baath, L. B., & Johansson, L. E. B. 1988, *ApJ*, 325, 382
- Novak, G., Dotson, J. L., Dowell, C. D., Goldsmith, P. F., Hildebrand, R. H., Platt, S. R., & Schleuning, D. A. 1997, *ApJ*, 487, 320
- Novak, G., Gonatas, D. P., Hildebrand, R. H., Platt, S. R., & Dragovan, M. 1989, *ApJ*, 345, 802
- Plambeck, R. L., Wright, M. C. H., Mundy, L. G., & Looney, L. W. 1995, *ApJ*, 455, L189
- Platt, S. R., Dotson, J. L., Dowell, C. D., Hildebrand, R. H., Schleuning, D., & Novak, G. 1995, in ASP Conf. Proc. 73, Proc. of the Airborne Astronomy Symp. on the Galactic Ecosystem: From Gas to Stars to Dust, ed. M. R. Haas, J. A. Davidson, & E. F. Erickson (San Francisco: ASP), 543
- Platt, S. R., Hildebrand, R. H., Pernic, R. J., Davidson, J. A., & Novak, G. 1991, *PASP*, 103, 1193
- Purcell, E. M. 1979, *ApJ*, 231, 404
- Roberge, W. G. 1996, in ASP Conf. Proc. 97, Polarimetry of the Interstellar Medium, ed W. G. Roberge & D. B. Whittet (San Francisco: ASP), 401
- Roberts, D. A., Crutcher, R. M., & Troland, T. H. 1996, in ASP Conf. Proc. 97, Polarimetry of the Interstellar Medium, ed W. G. Roberge & D. B. Whittet (San Francisco: ASP), 527
- Schleuning, D. A., Dowell, C. D., Hildebrand, R. H., Platt, S. R., & Novak, G. 1997, *PASP*, 109, 307
- Schleuning, D. A., Dowell, C. D., & Platt, S. R. 1996, in ASP Conf. Proc. 97, Polarimetry of the Interstellar Medium, ed. W. G. Roberge & D. B. Whittet (San Francisco: ASP), 285
- Shu, F. H., Adams, F. C., & Lizano, S. 1987, *ARA&A*, 25, 23
- Stacey, G. J., Jaffe, D. T., Geis, N., Genzel, R., Harris, A. I., Poglitsch, A., Stutzki, J., & Townes, C. H. 1993, *ApJ*, 404, 219
- Tauber, J. A., Tielens, A. G. G., Meixner, M., & Goldsmith, P. F. 1994, *ApJ*, 422, 136
- Tielens, A. G. G. M., & Hollenbach, D. 1985b, *ApJ*, 291, 747
- Troland, T. H., Heiles, C., & Goss, W. M. 1989, *ApJ*, 337, 342
- Vrba, F. J., Strom, S. E., & Strom, K. M. 1988, *AJ*, 96, 680
- Van der Werf, P. P., & Goss, W. M. 1989, *A&A*, 224, 209
- Werner, M. W. 1982, in Ann. NY Acad. Sci., 395, Symp. on the Orion Nebula to Honor Henry Draper, ed. A. E. Glassgold, P. J. Huggins, & E. L. Schucking, 79
- Wright, M., Sandell, G., Wilner, D. J., & Plambeck, R. L. 1992, *ApJ*, 393, 225